Optical Engineering

OpticalEngineering.SPIEDigitalLibrary.org

Development of a concave freeform surface measurement using transverse translation-diverse phase retrieval

Aaron M. Michalko
James R. Fienup

SPIE.

Aaron M. Michalko, James R. Fienup, "Development of a concave freeform surface measurement using transverse translation-diverse phase retrieval," *Opt. Eng.* **59**(6), 064101 (2020), doi: 10.1117/1.OE.59.6.064101

Development of a concave freeform surface measurement using transverse translation-diverse phase retrieval

Aaron M. Michalko* **and James R. Fienup**
University of Rochester, Institute of Optics, Rochester, New York, United States

Abstract. Transverse translation-diverse phase retrieval (TTDPR), a ptychographic wavefront-sensing technique, is a viable method for freeform optical surface metrology due to its relatively simple hardware requirements, flexibility, and demonstrated accuracy in other fields. In TTDPR, a subaperture illumination pattern is scanned across an optic under test, and the reflected intensity is gathered on an array detector near focus. A nonlinear optimization algorithm is used to reconstruct the wavefront aberration at the test surface from which we can solve for surface error, using intensity patterns from multiple scan positions. TTDPR is an advantageous method for aspheric and freeform metrology because measurements can be performed without null optics. We report on the development of a concave freeform mirror measurement using this technique. Simulations were performed to test algorithmic performance as a function of various parameters, including detector signal-to-noise ratio and position uncertainty of the illumination, with $<\lambda/100$ root-mean-square (rms) wavefront-sensing error achieved in most cases ($\lambda = 632.8$ nm). An experimental measurement is then demonstrated, and results of reconstructed surface form and midspatial frequency error are presented. Surface reconstructions from two disjoint datasets agree to 13-nm rms, or $\lambda/50$ at $\lambda = 632.8$ nm. © *2020 Society of Photo-Optical Instrumentation Engineers (SPIE)* [DOI: 10.1117/1.OE.59.6.064101]

Keywords: phase retrieval; surface metrology; freeform metrology; wavefront sensing.

Paper 20200278 received Mar. 6, 2020; accepted for publication May 18, 2020; published online Jun. 1, 2020.

1 Introduction

Freeform optical surfaces, i.e., surface descriptions that lack rotational symmetry, are a powerful technology due to their flexibility and aberration-correcting capabilities. However, optical metrology of freeform surfaces remains challenging. Unlike conic surfaces, freeforms generally do not possess a stigmatic imaging configuration that would facilitate an interferometric null test. Rather, the slope departure of a freeform shape from a base sphere can create unresolvable test fringes on the detector of an interferometer in addition to introducing retrace errors. To overcome these challenges, additional optics may be introduced, such as a computer-generated hologram or custom null optics,[1] or subaperture stitching may be used.[2] Often, these methods tend to be expensive and require complicated additional hardware to take a measurement.[2] We are interested in an alternative metrology approach suitable for freeform surface characterization with significantly reduced hardware requirements and associated cost.

One suitable technique is transverse translation-diverse phase retrieval (TTDPR), a ptychographic[3] method of image-based wavefront sensing.[4–7] TTDPR is an attractive technique for optical surface metrology, particularly concave surface metrology, due to its relatively simple hardware requirements.[8,9] Using TTDPR, measurements of concave surfaces may only require a source, a translating mask, and an array detector. A TTDPR measurement does not require additional reference or imaging optics, reducing the cost and uncertainties associated with manufacturing and calibrating those optics. In addition, TTDPR does not suffer from retrace errors when measuring an aspheric wavefront and is suitable to measure aspheric and freeform optics without needing additional null optics.

*Address all correspondence to Aaron M. Michalko, E-mail: aaronmichalko@gmail.com

In this paper, we discuss the development of an optical measurement utilizing TTDPR. In Sec. 2, we will discuss the computational forward model used to (1) reconstruct an unknown wavefront aberration function and (2) calculate the surface topography error of an optical surface using the reconstructed wavefront aberration function. In Sec. 3, we present a series of computer simulations to investigate both the wavefront-sensing accuracy of TTDPR in the presence of large aberrations and the accuracy of the surface error calculations. In Sec. 4, we discuss the results of a laboratory measurement of a concave freeform mirror.

2 Measurement Model

2.1 *Exit Pupil Field Reconstruction*

TTDPR is a method for reconstructing a complex field of interest using intensity patterns measured near a focus of the field of interest. In TTDPR, a subaperture portion of the field of interest is illuminated and the corresponding intensity pattern is measured on an array detector. The subaperture illumination pattern is then moved to a number of discrete, overlapping locations and intensities are gathered at each position. These measured intensity patterns are then compared to intensities of computer-propagated fields from an estimate of the optical field of interest. The estimate of the field is iteratively updated to optimize the agreement between the predicted intensities and the measured ones until a final prediction of the full complex field, amplitude and phase, is obtained.

In the context of optical testing, the field of interest is often located in an exit pupil and modeled by a generalized pupil function[10]

$$g(x_p, y_p) = |g(x_p, y_p)| \exp\left[\frac{i2\pi}{\lambda} W(x_p, y_p)\right], \tag{1}$$

where λ is the source wavelength and $W(x_p, y_p)$ is the unknown wavefront aberration we want to characterize, expressed in pupil coordinates (x_p, y_p). Here, $W(x_p, y_p)$ has units of length and is interpreted as the optical path difference between the aberrated wavefront in the exit pupil and a reference sphere centered on an ideal image point.[10] For transmitted wavefront testing of an optical element,[4] the exit pupil may be defined in a plane just past the optic. A physical translating subaperture structure can be placed directly in the exit pupil plane to transmit a subaperture portion of the field. For optical surface testing, we define an exit pupil near the surface under test and instead take measurements in reflection. Because a physical subaperture structure placed at or near the surface may obscure portions of the reflected beam or possibly damage the surface, translating subaperture illumination can instead be achieved by projecting an illumination pattern onto the surface under test.[8] Figure 1(a) illustrates the particular measurement geometry under investigation in this work. Figure 1(b) shows the relationships between pupil coordinates, (x_p, y_p), surface coordinates, (x_s, y_s), and coordinates before reflection, (x, y). The coordinates (x, y) are normal to the nominal optical axis before reflection, and the coordinates (x_p, y_p) are normal to the optical axis after reflection. All three coordinate systems share a common origin at the center of the surface, which we call the surface origin. A freeform surface with nominal surface height $z_N(x_s, y_s)$, where $z_N(0,0) = 0$, is illuminated by a point source positioned at a distance z_2 from the surface origin as measured along the nominal optical axis before reflection. A clipping mask placed between the source and the surface at a distance z_1 from the source creates the subaperture illumination pattern. The surface is tilted by a nominal angle θ, which serves two purposes. First, it clears the reflected beam from obstruction by the mask or detector. Second, the tilt-induced astigmatism may be used to partially null the surface-induced astigmatism by a particular freeform. Reflected intensities are then collected by an array detector positioned at a distance z_o from the surface origin along the nominal optical axis after reflection. We define an exit pupil reference sphere with radius z_o, centered on the intersection of the nominal optical axis with the detector, to define $W(x_p, y_p)$. In this work, we explore a specific configuration where z_2 and z_o are both approximately equal to the surface radius of curvature.

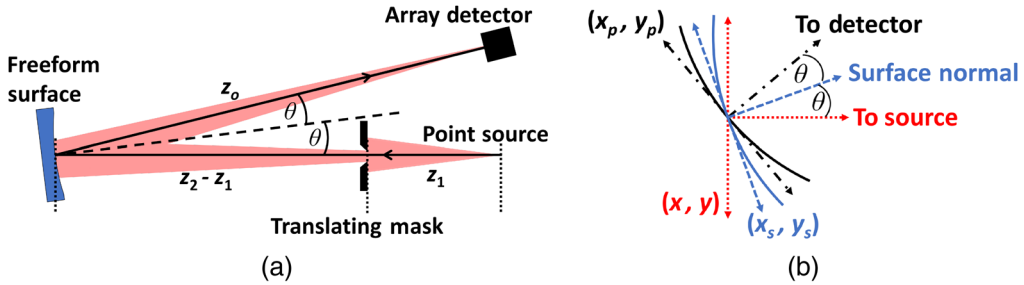

Fig. 1 (a) Proposed test configuration for freeform surface measurement. The nominal optical axis is indicated by a solid black line. Dotted black lines indicate positions of source, mask, and surface origin along the optical axis. (b) Local coordinate systems. Dotted red: Coordinate axes, (x, y), normal to optical axis before reflection. Dashed blue: Local surface coordinate axes (x_s, y_s). Solid blue: Surface under test $z(x_s, y_s)$. Dash-dotted black: Exit pupil coordinate axes (x_p, y_p). Solid black: The exit pupil reference sphere.

In general, both z_2 and z_o may take different values, which may be advantageous depending on the best-fit conic to the surface under test or geometrical constraints.

It is important to note that in this candidate test geometry, the concept of an underlying exit pupil field at the surface is a notional one. At no time is the entire surface illuminated, so at no time is the entire pupil field realized. However, it is mathematically useful to construct $g(x_p, y_p)$ so that we can separate effects that are due to the changing illumination pattern from effects due to the static alignment of the optic. Although it is not investigated in this work, the translating subaperture may be placed after the surface under test instead of before, as long as that configuration is correctly modeled in the phase retrieval algorithm. In that case, the exit pupil field would be physically realized.

The unknown wavefront aberration function $W(x_p, y_p)$ is often parameterized using a weighted sum of basis polynomials, such as Zernike polynomials,[11] to efficiently model the dominant low-order surface figure errors expected from the optical fabrication process. However, aspheric and freeform optics are often fabricated using subaperture grinding, polishing, or turning techniques, which leave behind characteristic midspatial frequency (MSF) surface errors. Zernike polynomials are limited in their ability to reconstruct MSF features with high accuracy, possibly requiring tens of thousands of terms.[12] To avoid the requirement for very large numbers of basis polynomials, which could become computationally expensive, we adopt the following wavefront parametrization:

$$W(x_p, y_p) = \sum_j a_j Z_j(x_p, y_p) + [P(x_p, y_p) * K(x_p, y_p)], \tag{2}$$

where $Z_j(x_p, y_p)$ is the j'th Zernike polynomial with weight a_j to model low-order wavefront errors. The function $P(x_p, y_p)$ is a point-by-point (PBP) varying phase, $*$ denotes convolution, and $K(x_p, y_p)$ is a convolution kernel. By changing the width of $K(x_p, y_p)$, we can control the spatial frequency bandwidth of $W(x_p, y_p)$, allowing us to model MSF and higher spatial frequency features. The convolution model is an application of the "method of sieves."[13] This is a form of bootstrapping, estimating the lower-frequency phases first using a wide kernel, and progressing to higher-frequency phases using narrower kernels. This is an improvement over a PBP-only phase, which can be prone to algorithmic stagnation or overfitting to the noise.

Next, we introduce a complex-valued, translating subaperture illumination function $A_k(x_p, y_p)$. In some cases, we may assume that $A_k(x_p, y_p)$ can be modeled using a simple translation, i.e.,

$$A_k(x_p, y_p) = A(x_p - x_k, y_p - y_k), \tag{3}$$

where $A(x_p, y_p)$ is a global subaperture function and (x_k, y_k) is the subaperture translation. In other cases, depending on the measurement geometry, the subaperture illumination function may change size or shape as it is moved across the exit pupil. In this paper, a subaperture model

according to Eq. (3) is used in Secs. 3.2–3.4. A more general subaperture model, in which the shape of $A_k(x_p, y_p)$ is recalculated for each position, is used in Secs. 3.5 and 4.

The width of $A_k(x_p, y_p)$ should be sized to produce well-sampled intensities, where sampling is expressed in terms of the sampling ratio[14]

$$Q = \frac{\lambda z_o}{D\Delta_u}, \tag{4}$$

where λ is the test wavelength, z_o is the propagation distance, Δ_u is the detector pixel pitch, and D is the physical width of A_k in the exit pupil. Here, $Q = 2$ corresponds to Nyquist-sampled intensities. By scanning the subaperture across the field of interest, we are able to take well-sampled measurements over a much larger effective diameter than would be possible using a full-aperture phase retrieval technique, such as focus-diverse phase retrieval.

For each illumination position, the field transmitted through the exit pupil can be modeled as

$$g_k(x_p, y_p) = A_k(x_p, y_p)g(x_p, y_p). \tag{5}$$

The field incident on the detector is then calculated using

$$G_k(u, v) = P[g_k(x_p, y_p)], \tag{6}$$

where P is an appropriate propagator. In this work, we assume that the field at the detector plane is related to the general pupil function through Fraunhofer propagation, which can be written in discrete form

$$\boldsymbol{G}_k[m_r, m_c] \propto \sum_{n_r=0}^{N-1}\sum_{n_c=0}^{N-1} \boldsymbol{g}_k[n_r, n_c] \exp\left[-i2\pi\left(\frac{\Delta_u\Delta_x}{\lambda z_\circ}\right)(n_c m_c + n_r m_r)\right], \tag{7}$$

where $\boldsymbol{G}_k$ is the size $M \times M$ discretized detector field with row and column indices $[m_r, m_c]$ and pixel pitch Δ_u. Here, $\boldsymbol{g}_k$ is the size $N \times N$ discretized pupil field with row and column indices $[n_r, n_c]$ and simulated pixel pitch Δ_x.

The model for detected intensity is then

$$\boldsymbol{I}_k[m_r, m_c] \propto |\boldsymbol{G}_k[m_r, m_c]|^2. \tag{8}$$

Note that in Eq. (7) we dropped a leading quadratic phase term that would be suppressed by Eq. (8).

Simulated intensities were then compared to measured intensities, $\boldsymbol{D}_k$, using a normalized mean-squared error metric

$$E = \frac{\sum_k \sum_{m_r,m_c} \boldsymbol{w}_k[m_r, m_c]\{\boldsymbol{D}_k[m_r, m_c] - (\gamma_k \boldsymbol{I}_k[m_r, m_c] + \beta_k)\}^2}{\sum_k \sum_{m_r,m_c} \boldsymbol{w}_k[m_r, m_c]\boldsymbol{D}_k[m_r, m_c]^2}, \tag{9}$$

where $\boldsymbol{w}_k$ is a weighting function that can be used to suppress information from bad pixels, γ_k is a gain parameter, and β_k is a bias parameter. Here, γ_k and β_k were calculated using Eq. (C3) in Ref. 7 so that the gradient of E with respect to both γ_k and β_k is 0, thus making E insensitive to detector gain and bias.

We are tasked with minimizing the value of E with respect to experimental parameters. For this work, nonlinear optimization was performed using an L-BFGS optimizer[15] in Python. Gradients with respect to various test parameters were calculated using algorithmic differentiation techniques.[7,16]

2.2 *Surface Error Calculation from Reconstructed Wavefront Aberration*

After reconstructing $W(x_p, y_p)$ using TTDPR, we must next calculate the sag error of the surface under test

$$\delta z(x_s, y_s) = z(x_s, y_s) - z_N(x_s, y_s), \tag{10}$$

where $z(x_s, y_s)$ is the true surface height and $\delta z(x_s, y_s)$ is the unknown sag error from nominal, represented in surface coordinates (x_s, y_s). We first calculate the measured change in the wavefront aberration from nominal as

$$\delta W(x_p, y_p) = W(x_p, y_p) - W_N(x_p, y_p). \tag{11}$$

The values of $W_N(x_p, y_p)$, the nominal wavefront aberration, are obtained using a ray trace model of an idealized measurement configuration, where the surface under test is the nominal surface. A set of rays, termed "nominal rays," are traced to the exit pupil reference sphere, and each value of $W_N(x_p, y_p)$ is the difference between the optical path length of the nominal ray that intersects the reference sphere at (x_p, y_p) and the optical path length of the nominal ray that intersects the reference sphere at (0, 0). Each nominal ray will also intersect the nominal surface, and assuming both the surface and the reference sphere are far from a region of nominal ray caustics, there is a one-to-one mapping between nominal ray surface intersections and nominal ray reference sphere intersections, given as

$$(x_{r,s}, y_{r,s}) = f(x_p, y_p), \tag{12}$$

where $(x_{r,s}, y_{r,s})$ are the surface intersection coordinates of the nominal ray that intersects the reference sphere at (x_p, y_p) and f is the mapping function. In our work, the values of $f(x_p, y_p)$ are found numerically using nominal ray traces.

If δz is small, which is a reasonable assumption in our metrology application, we can use a perturbation approximation to relate surface sag error to the change in wavefront aberration.[17,18] To first order, this relationship is given as

$$\delta W(x_p, y_p) = -2\delta z_\perp(x_{r,s}, y_{r,s}) \cos[\theta_i(x_{r,s}, y_{r,s})], \tag{13}$$

where $\delta W(x_p, y_p)$ is the induced change in wavefront aberration, $\theta_i(x_{r,s}, y_{r,s})$ is the angle of incidence of the nominal ray that intersects the surface at $(x_{r,s}, y_{r,s})$, and $\delta z_\perp$ is the projection of δz onto the nominal surface normal vector,

$$\delta z_\perp(x_s, y_s) = \delta z(x_s, y_s) \sqrt{1 - \left[\frac{\partial z_N(x_s, y_s)}{\partial x}\right]^2 - \left[\frac{\partial z_N(x_s, y_s)}{\partial y}\right]^2}. \tag{14}$$

An advantageous property of Eq. (13) is that all quantities except δW depend on the nominal rays or the nominal surface and can be numerically calculated using a ray trace. Furthermore, Eq. (13) accounts for the coordinate mapping between the exit pupil, where $W(x_p, y_p)$ is defined, and the optical surface, where sag error is defined. It is important to understand this mapping, especially if measured surface data are used for closed-loop feedback into fabrication processes. Otherwise, surface error incorrectly attributed to one region of the part may be left uncorrected or even exacerbated by attempts to fix it through deterministic polishing. A similar type of mapping problem exists in other off-axis test methods, such as interferometric null testing, where the plane of the interferogram may be tilted relative to the local coordinates of the surface under test.

3 Computer Simulations

A series of computer simulations were performed to investigate the performance of TTDPR in realistic testing scenarios for freeform optics. These simulations were motivated by the selection of a candidate freeform test mirror: the secondary mirror from a three-mirror, freeform, thermal imaging system.[1,19,20] The mirror is a base sphere plus an approximate 120-μm peak-to-valley (P–V) freeform sag, as shown in Fig. 2. The nominal surface, including the base sphere, has a maximum sag from flat of ~1.9 mm.

Sections 3.1–3.4 contain simulations that probe the wavefront-sensing accuracy of TTDPR, corresponding to the methods in Sec. 2.1. Section 3.5 contains end-to-end simulations to validate

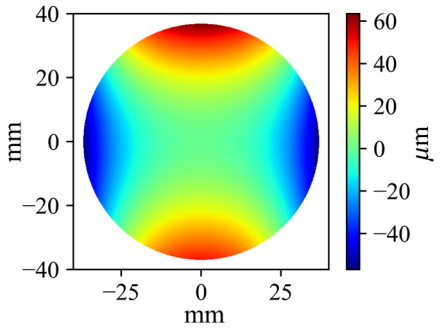

Fig. 2 Freeform mirror nominal sag departure from a base sphere, shown over a 74-mm-diameter circular region.

the entire metrology method, including both wavefront reconstructions from Sec. 2.1 and surface error calculations from Sec. 2.2.

3.1 *Wavefront-Sensing Accuracy with Noisy Data*

First, simulations were performed to explore the effect of simulated detector noise on TTDPR wavefront-sensing accuracy. A series of wavefront aberrations were simulated based on a CODE V ray-trace model of the tilted freeform mirror with a tilt angle of $\theta = 7$ deg, made to avoid obscuration of the reflected intensities. A total of 36 nominal Zernike wavefront coefficients were generated using CODE V, and these coefficients were exported to a TTDPR algorithm and used as the a_j in Eq. (2) for simulating the wavefront from the ideal (nominal) surface under test. No additional PBP phase was simulated. This nominal wavefront aberration was defined over a circular clear aperture and had a P–V of 305.4λ and a root-mean-square (rms) of 60.9λ, with piston, tip, and tilt (PTT) removed, at the simulated test wavelength of 632.8 nm. To the nominal wavefront aberration, a 4.0λ rms perturbation was added using a random superposition of 20 Zernike polynomials (through the fifth radial order). This perturbation represented unknown errors caused by fabrication defects.

For these simulations, subaperture illumination was modeled using Eq. (3). The global subaperture function $A(x_p, y_p)$ was modeled using a hard-edged circular subaperture with a diameter equal to 20% of the underlying pupil diameter. This simplified illumination model was sufficient to explore the algorithmic performance of TTDPR. Later, for laboratory measurements of a freeform surface in Sec. 4, a more physically realistic model for A_k was used that included diffraction effects. To achieve good coverage over the entire simulated wavefront function, 77 illumination translations, (x_k, y_k), were simulated and arranged in a concentric ring pattern as shown in Fig. 3. Subaperture translations were intentionally selected so that some A_k would overlap the clipping edge of the pupil. To accommodate the noninteger pixel values of x_k and y_k, bilinear interpolation was used in this work.[7]

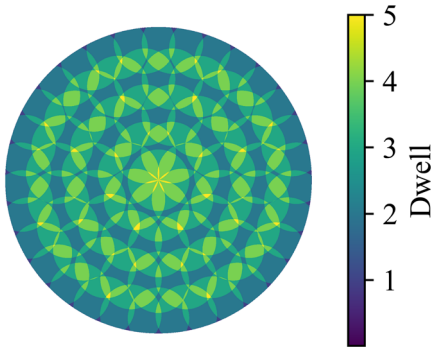

Fig. 3 Superposition of subaperture positions. Color bar value indicates the number of times an area of the pupil was sampled.

Nyquist-sampled intensities were modeled and detector noise was generated using a combined Gaussian and Poisson noise model, using 16 electrons rms Gaussian read noise and varying peak pixel photons. Ten simulations, each having different noise realizations and wavefront perturbations, were performed for each peak photoelectron level. Owing to the large underlying aberrations, the centroid of each intensity pattern wandered significantly over the simulated detector region. To avoid simulating intensity patterns with large regions of noise, simulated fields g_k were multiplied by a linear phase term in the forward model that shifted the intensity pattern to the center of a simulated 512×512 pixel detector region. Information about the position of each intensity pattern on the detector was preserved according to the Fourier shift theorem. This process is analogous to measuring the intensities on a large array detector in the lab and cropping each intensity to a given size about a new center pixel. From the distance between the new center pixel and the detector origin, one can calculate a corresponding linear phase to multiply each g_k. Example intensities are shown in Fig. 4.

In our nonlinear optimization, 35 Zernike polynomial coefficients were optimized using the nominal wavefront as the starting guess (piston ignored). After optimization, $\delta W(x_p, y_p)$ was calculated according to Eq. (11). Let $\boldsymbol{\delta W}[n_r, n_c]$ be the discrete array representation of $\delta W(x_p, y_p)$ and let $\boldsymbol{m}[n_r, n_c]$ be a binary array corresponding to the nonzero area of $|g(x_p, y_p)|$. Root-mean-square wavefront-sensing error (rms WFSE) was then calculated using

$$rms\text{WFSE} = \sqrt{\frac{\sum_{n_r,n_c} \boldsymbol{\delta W}[n_r, n_c]^2 \boldsymbol{m}[n_r, n_c]}{\sum\limits_{n_r,n_c} \boldsymbol{m}[n_r, n_c]}}. \tag{15}$$

Figure 5 shows rms WFSE versus peak pixel photons for the simulated cases. For cases with 10,000 peak photons or greater, the algorithm could reliably converge with rms error on the order

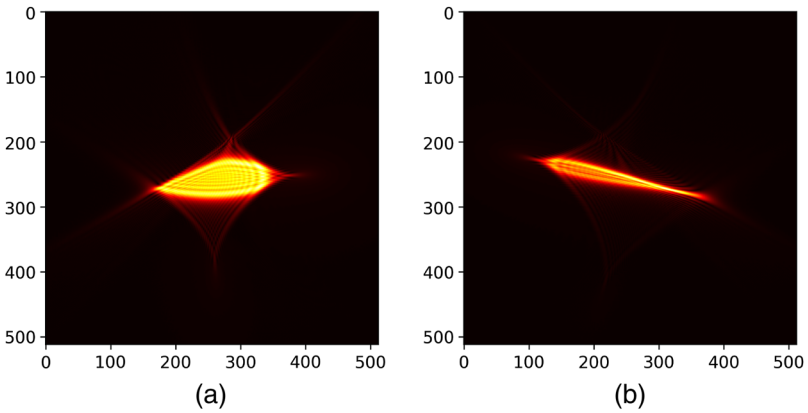

Fig. 4 Example simulated nominal intensities from $\theta = 7$ deg wavefront. Intensities are shown raised to a power of 1/2 with no simulated detector noise and are shown shifted to the center of the array. Axes are labeled by pixel index.

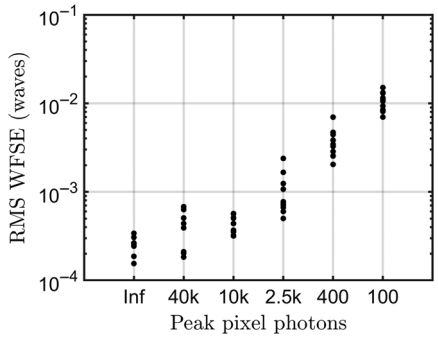

Fig. 5 Residual rms WFSE versus peak pixel photons with 16-electron rms read noise.

of $\lambda/1000$. rms error $< \lambda/100$ was achievable with as few as 400 peak photons. These signal powers are easily obtainable in the lab, thus we expect detector noise alone to affect the accuracy of TTDPR very little in a laboratory testing environment. Additional simulations were performed with fully noise-free intensities, which would allow for model-matched solutions, and rms errors were obtained on the order of $\lambda/5000$. Furthermore, for all simulated cases, the algorithm always converged to a solution and did not stagnate, indicating a large capture range compared to other phase retrieval methods such as focus-diverse phase retrieval.[21]

3.2 *Transverse Translation-Diverse Phase Retrieval with Known Defocus*

Next, TTDPR wavefront-sensing accuracy was tested in the presence of varying amounts of known defocus, because it has been shown that phase retrieval for wavefront sensing can sometimes benefit from the addition of defocus to the nominal wavefront.[22–25] For testing well-corrected optical systems, additional defocus spreads the otherwise narrow intensity distribution over a larger region on the detector, leading to a greater number of high-signal-to-noise ratio (SNR) pixels that contribute to E. However, in freeform optical testing, the measured intensity distributions are, in general, many times larger than the diffraction limit due to the underlying surface shape of the optic and lack of a simple null configuration.

To test the performance of TTDPR with respect to known defocus, simulations were performed using the forward model parameters described in Sec. 3.1. For each simulation, a known amount of Zernike defocus was added to the nominal wavefront. Defocus magnitudes ranged from 0 to 64λ P–V. Such values could be attained in the lab by translating the detector along the optical axis or by inserting a weakly powered optical element into the beam path. Defocused intensities were simulated with 16-electron rms Gaussian read noise and 40,000 peak pixel photons.

Figure 6 shows WFSE versus defocus for the simulations performed. rms WFSE $< \lambda/1000$ was observed over the entire range of simulations with no strong functional dependence observed. This is most likely caused by the large aberration contribution of the nominal wavefront. Even with no additional defocus, the simulated intensities have energy spread over many pixels, contributing strongly to reducing the error metric.

3.3 *Transverse Translation-Diverse Phase Retrieval with Subaperture Positioning Error*

Next, the accuracy of TTDPR was explored with respect to errors in the position of the subaperture illumination. Errors in subaperture position may occur in the lab as a result of calibration errors or systematic errors from the stages used to translate the moving mask. Joint retrieval of subaperture position along with wavefront error has been previously demonstrated using TTDPR for mildly aberrated systems.[4,6,7,26,27] We are interested in how uncertainties in subaperture position will affect the freeform case, where aberrations are, in general, much larger. We performed simulations using two nominal wavefronts, corresponding to two different tilt

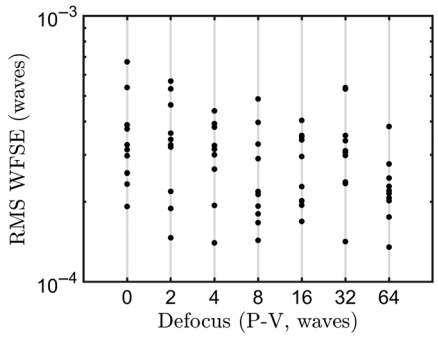

Fig. 6 Residual rms WFSE versus known defocus. For a large range of known defocus values, phase was retrieved with sub-$\lambda/1000$ rms residual error.

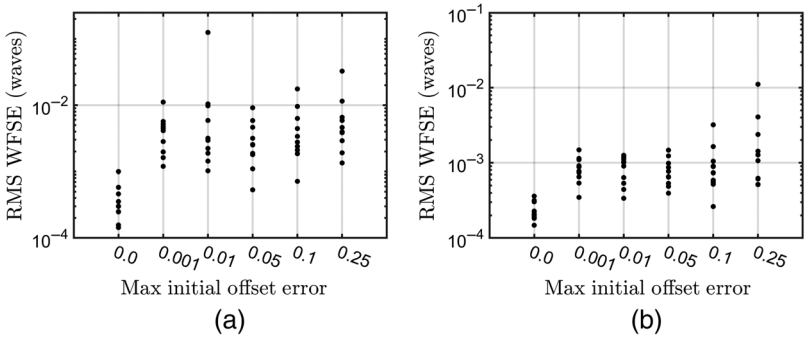

Fig. 7 Residual rms WFSE versus size of initial offset error distribution, corresponding to mirror tilt angles of (a) $\theta = 7$ deg and (b) $\theta = 13.91$ deg. Initial offset errors were drawn from a uniform random distribution over a disk, whose radius was specified as a fraction of the total subaperture width.

angles of the freeform mirror under test. In addition to the $\theta = 7$ deg nominal wavefront aberration, simulations were performed using $\theta = 13.91$ deg. Here $\theta = 13.91$ deg is the angle at which tilt-induced astigmatism nulls nominal surface-induced third-order astigmatism, according to the Coddington trace equations. [28,29] The resulting wavefront aberration has a P–V of 67.7λ and an rms of 15.9λ over the simulated area of interest with PTT removed.

For these simulations, wavefronts and data were again simulated according to the process described in Sec. 3.1 with 40,000 simulated peak pixel photons. However, for these simulations, the initial guess for each subaperture translation was perturbed by a random offset. The random offset errors were drawn from a uniform distribution over a disk with a specified radius. The radius of this distribution varied from 0% to 25% of the subaperture width. In optimization, 35 Zernike coefficients were first optimized with fixed (yet incorrect) translations. Next, all subaperture translations were optimized jointly with the wavefront coefficients. All other parameters except translations and Zernike coefficients were assumed known.

Figure 7 shows WFSE versus subaperture offset error for both nominal wavefronts. Compared to Figs. 5 and 6, Fig. 7(a) shows a larger mean and variance of WFSE, with the singular worst case resulting in $\approx 0.12\lambda$ rms WFSE, [the uppermost point in Fig. 7(a)], which was found to be dominated by a linear phase error. Once the linear phase component had been removed from that result, the residual WFSE was reduced to $\approx \lambda/50$. However, the ensemble performed well overall, with 54/60 cases resulting in $<\lambda/100$ rms WFSE. Fig. 7(b) shows lower overall error, with 59/60 cases resulting in $<\lambda/100$ rms WFSE and the majority resulting in $<\lambda/1000$ rms for translation errors up to 10% the subaperture diameter. Although uncertainty in subaperture translation will cause additional uncertainty in the final wavefront reconstructions, these results show that successful retrievals are still possible with random offset errors up to 25% the subaperture diameter. In a well-controlled laboratory environment, expected offset errors should be much less than 25%. In a testing environment, calibration should be performed to minimize offset errors, but there are additional paths toward developing a more robust test in the presence of unknown offset errors. One may be developing a better optimization strategy in which we more strictly control when and how the subaperture translations vary in optimization.[7] It may also be advantageous to introduce known amplitude structures in the optical aperture that would serve as position references for the translating illumination, since we can reconstruct both the amplitude and phase of the optical field.

3.4 *Transverse Translation-Diverse Phase Retrieval with Errors in the Sampling Parameter*

As shown in Eq. (7), simulated fields were propagated using a discrete Fraunhofer propagation, which is accomplished with a discrete Fourier transform (DFT). TTDPR performance was tested in the presence of errors in the DFT sampling parameter, α, given as

$$\alpha = \frac{\Delta_u \Delta_x}{\lambda z_o}. \tag{16}$$

Here, α must be selected for the experiment to ensure that simulated intensities are not aliased by the wraparound nature of the DFT. α relates to Q, as defined in Eq. (4), as

$$\alpha = \frac{\Delta_x}{QD}. \tag{17}$$

From a practical perspective, uncertainties in α are directly linked to uncertainties in the physical experimental parameters in Eq. (16). Therefore, an exploration of TTDPR performance in the presence of errors in α may help inform an error budget on those physical terms. Previous work regarding reconstructing α demonstrated high accuracy but dealt with 0.1λ rms wavefronts using focus-diverse phase retrieval.[30] We are interested in the performance of TTDPR with highly aberrated wavefronts that we would expect from freeform testing. In this work, both the matrix-product DFT[31] and chirp Z-transform[30] were used instead of a fast Fourier transform (FFT). This allows α to take on any value, rather than the value $1/N$, where N is the number of pixels in the input array, the FFT constraint.

For these simulations, wavefronts and data were again simulated according to the process in Sec. 3.1 with 40,000 peak photons. However, in these simulations, α was allowed to vary during optimization along with the 35 Zernike coefficients. All other parameters were assumed known. Data were simulated using the true sampling parameter, α_{true}, but the starting guess, α_{init}, was perturbed by a prescribed amount relative to the truth. In these simulations, both α and coefficients a_j were jointly optimized from the start. After optimization, estimates of both the wavefront coefficients and the sampling parameter, α_{rec}, were obtained, and rms WFSE was calculated.

Figures 8(a) and 8(b) show rms WFSE versus fractional error in the initial value of the sampling parameter $|(\alpha_{\text{init}} - \alpha_{\text{true}})/\alpha_{\text{true}}|$. As shown in Fig. 8(a), the more highly aberrated wavefront was more sensitive to errors in α, with 48/60 simulations resulting in rms WFSE $<\lambda/100$. For the less aberrated case, where $\theta = 13.91$ deg, 60/60 simulations resulted in rms WFSE $<\lambda/100$

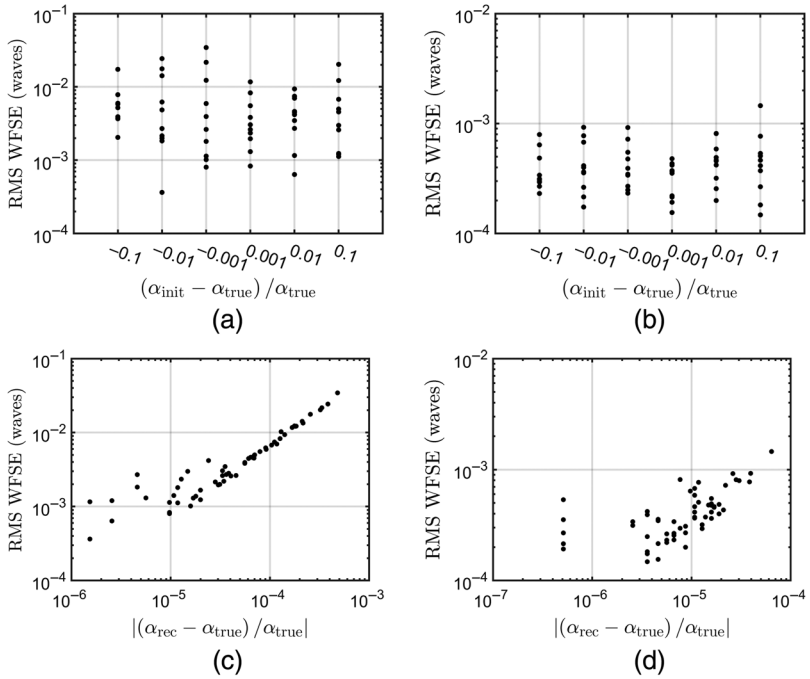

Fig. 8 rms WFSE versus error in the initial sampling parameter $(\alpha_{\text{init}} - \alpha_{\text{true}})/\alpha_{\text{true}}$ for (a) $\theta = 7$ deg and (b) $\theta = 13.91$ deg. rms WFSE versus error in the reconstructed sampling parameter $|(\alpha_{\text{rec}} - \alpha_{\text{true}})/\alpha_{\text{true}}|$ for (c) $\theta = 7$ deg and (d) $\theta = 13.91$ deg.

and 59/60 simulations resulted in rms WFSE $<\lambda/1000$. In both cases, TTDPR performance did not appear to depend strongly on the specific value of α_{init}. To better understand these results, residual rms WFSE was compared to the fractional error in the reconstructed sampling parameter $|(\alpha_{\text{rec}} - \alpha_{\text{true}})/\alpha_{\text{true}}|$, shown in Figs. 8(c) and 8(d). The following regression was calculated using the data in Fig. 8(c)

$$rms\ \text{WFSE(waves)} \approx 64.84 \left| \frac{\alpha_{\text{rec}} - \alpha_{\text{true}}}{\alpha_{\text{true}}} \right| + 0.0005, \tag{18}$$

with $R^2 = 0.987$. Neglecting the small constant term, Eq. (18) illustrates that rms WFSE is proportional to fractional error in α_{rec} for $\theta = 7$ deg. Furthermore, the factor of proportionality is approximately equal to the nominal wavefront rms in waves. We can gain an intuition for this proportionality if we consider the phase retrieval system in terms of geometrical optics. According to geometrical optics, geometrical spot size is proportional to the magnitude of the wavefront aberration function. In the presence of large aberrations, e.g., $\theta = 7$ deg, the shapes of the measured intensities are dominated by geometrical effects. Because α acts as a DFT scaling parameter, an error in α may appear as if bright intensity regions have been geometrically magnified. This, in turn, may lead to local minima in optimization where the error in α is "corrected" by a proportional change in the magnitude of the wavefront aberration. However, the intensities will also possess high-spatial frequency features whose periodicity is dependent only on α, which appear only when diffraction is modeled. In the presence of large aberrations, those features can be orders of magnitude dimmer than the brightest intensity regions, so they may contribute relatively little to the nonlinear optimizer as it searches for a global minimum. However, the data in Fig. 8(d), corresponding to a less aberrated nominal wavefront, do not agree with a simple linear regression, suggesting that diffraction effects still contribute strongly to the shapes of those intensities. The magnitude of WFSEs in Fig. 8(d) are comparable to results from detector noise alone.

If TTDPR is being used to test a highly aberrated wavefront, and error in α is a concern, the capture range of α retrieval may be improved by probing the system in ways that allow diffraction effects to be a more dominant contributor to the recorded intensities. One approach may be to measure additional intensities with longer exposure times, where the brightest region is oversaturated, but the dimmer diffraction lobes have high SNR. A data mask, $\mathbf{w}_k$ in Eq. (9), can be applied in optimization to ignore the overexposed regions while fitting the dimmer ones. Alternatively, a second subaperture may be employed, such as a double pinhole, which would create a modified double-slit arrangement. The resulting intensities should contain a fringe pattern with a spatial frequency that depends on α.[4]

3.5 *Validation of Model and Surface Error Calculation*

Finally, end-to-end simulations were performed to validate the entire measurement process discussed in Sec. 2. Unlike the simulations described in Secs. 3.1–3.4, simulated intensity data were not generated by the TTDPR model used for wavefront reconstruction. Instead, for each subaperture position, noiseless intensities were first simulated using beamlet propagation in a CODE V model of a measurement configuration with $\theta = 13.91$ deg. For some simulations, detector noise was then simulated using Poisson noise with 40,000 peak photoelectrons and 16-photoelectron rms Gaussian read noise. The simulated data were supplied to the TTDPR algorithm to reconstruct first the wavefront aberration function and from it surface topography error. The translating subaperture illumination function and the underlying pupil amplitude were calculated according to Appendices A and B and used as priors in the TTDPR algorithm.

First, simulations were performed using intensity data generated from the nominal surface height. The nominal surface was reconstructed with a 0.7-nm RMS, 4.0-nm P–V error with PTT removed, both in simulations with and without simulated detector noise. The surface reconstruction error is most likely from a combination of systematic error in the TTDPR forward model and model mismatch between the TTDPR forward model and CODE V. However, it is small, on the order of $\lambda/1000$ rms at $\lambda = 632.8$ nm. Furthermore, in the simulation from noise-free intensities, TTDPR-predicted intensities differed from CODE V-simulated data by only 0.3% rms,

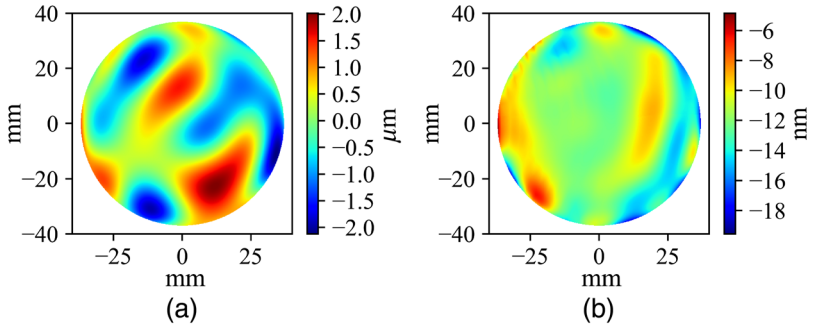

Fig. 9 (a) Simulated surface perturbation composed of 45 Zernike polynomials. This perturbation was added to the nominal surface prescription and intensities were simulated using beamlet propagation in ray-trace software. (b) Difference between the known perturbation and TTDPR-reconstructed surface with PTT removed. Note change in color bar scale from μm to nm.

indicating that the TTDPR forward model is suitably accurate for this application. Next, a 4.139-μm P–V, 0.866-μm rms surface perturbation, modeled using a superposition of 45 Zernike polynomials, as shown in Fig. 9(a), was added to the nominal mirror model in CODE V to simulate the presence of unknown manufacturing errors. Intensities were again generated in the ray-trace software and supplied to a TTDPR algorithm. The surface sag error was reconstructed and then differenced with the known simulated surface height, yielding a residual 1.1-nm rms, 11.0-nm P–V surface reconstruction error with PTT removed, as shown in Fig. 9(b). This error, although larger compared to the simulation from the nominal mirror model, is still small, $\approx\lambda/500$ rms, and demonstrates a successful end-to-end simulation of the proposed metrology method.

4 Laboratory Experiment

4.1 *Secondary Mirror Measurement*

After completing the simulations, the freeform mirror was measured experimentally using TTDPR in a tilted reflective geometry, as shown in Fig. 10. A red HeNe laser, $\lambda = 632.8$ nm, focused through a microscope objective/pinhole combination served as an effective point source. A circular transmission mask, mounted to two computer-controlled linear translation stages, was used to project a circular illumination pattern on the mirror. The mask was nominally positioned at a distance of 161.3 mm from the source and 221.4 mm from the surface origin. The circular mask had a nominal diameter of 6.35 mm and created a projected pattern on the part with an approximate diameter of 15.1 mm. The mirror was mounted to a custom kinematic base plate pair in a Kelvin clamp configuration.[29] This kinematic stage was used in a previous measurement of the freeform mirror using a custom optical null configuration consisting of two additional

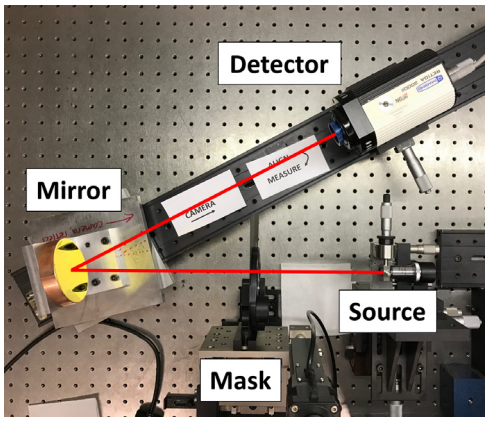

Fig. 10 Laboratory measurement configuration.

optical subsystems.[1] The bottom plate contains three milled conical seats spaced 120 deg apart, each holding a steel ball bearing. The top plate has three sets of three vee grooves, spaced 120 deg apart, designed to allow repeatable alignment to rotation angles of 0, $\theta = 13.91$ deg, and 2θ. The as-machined clocking angles corresponding to the θ and 2θ stage positions were measured to be 13.97 deg ± 0.01 deg and 27.95 deg ± 0.01 deg, respectively, using an autocollimator. To make these measurements, the top plate was removed and replaced nine times first at the nominal position, next at the θ position, next at the 2θ position, and last at the nominal position again to evaluate drift. For each set of nine angle measurements, rms positional repeatability was observed on the scale of 0.002 deg. The final reported measurement uncertainty of the stage angle was determined using the observed drift between the mean initial and final angle measurements of the stage at its nominal position.

TTDPR measurements were performed using data from two subaperture scan patterns gathered back to back: a concentric ring pattern similar to Fig. 3 and a Cartesian grid pattern, where the illumination was stepped linearly by distances of approximately 3.1 mm in each direction. For each translated position, the reflected intensity pattern was acquired with a QImaging Retiga-2000R CCD camera with a 7.4-μm pixel pitch, positioned a nominal distance $z_o = 382.6$ mm from the surface origin. Exposure was automatically adjusted between frames to use most of the camera's dynamic range, with typical exposure times on the order of tens of milliseconds. Figure 11 shows two sample data intensities. These data were then supplied to a TTDPR algorithm to reconstruct the wavefront aberration function according to the methods in Sec. 2.1. In the TTDPR forward model, translating subaperture illumination and pupil amplitude were modeled according to Appendices A and B.

Optimization was performed in multiple steps to avoid stagnation. First, optimization was performed while varying only tilt, power, and astigmatism terms in the wavefront. Next, 45 Zernike polynomial coefficients, the DFT sampling parameter, and illumination translations were jointly varied along with 45 Zernike coefficients. Next, low-order pupil amplitude polynomial coefficients were also varied, along with a PBP phase map used to model MSF features according to Eq. (2). A normalized raised-cosine wavefront convolution kernel was used

$$K(x_p, y_p) = \begin{cases} \frac{\pi}{L^2(\pi^2-4)}\left[1 + \cos\left(\frac{\pi}{L}\sqrt{x_p^2 + y_p^2}\right)\right], & \sqrt{x_p^2 + y_p^2} \le L \\ 0, & \text{else.} \end{cases} \tag{19}$$

Here, L is the full width at half maximum, which ranged from approximately $1/5$ to $1/64$ the subaperture illumination width, or approximately 3 to 0.24 mm.

After reconstructing the wavefront aberration, piston, tip-tilt, and power (PTTP) were removed using a least-squares fit over the area of the nonzero pupil amplitude. The filtered wavefront aberration was scaled and remapped to surface topography error using the methods described in Sec. 2.2. After remapping, PTTP were again removed from the reconstructed surface over a 74-mm-diameter circular region of interest.

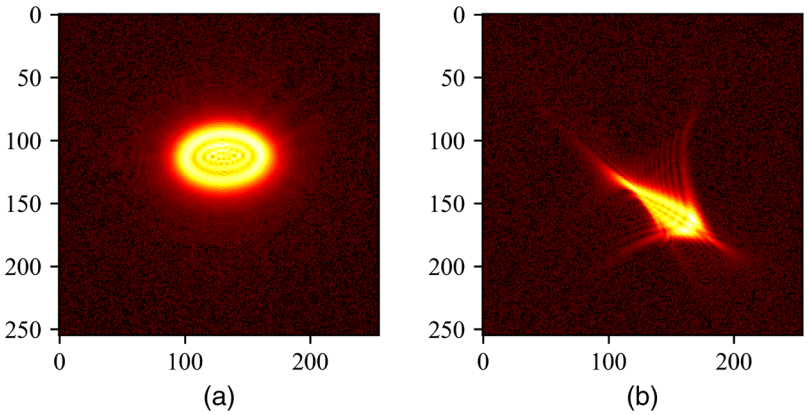

Fig. 11 Sample measured intensities, shown over a 256×256 region and raised to the 0.33 power. Axes are labeled by pixel index.

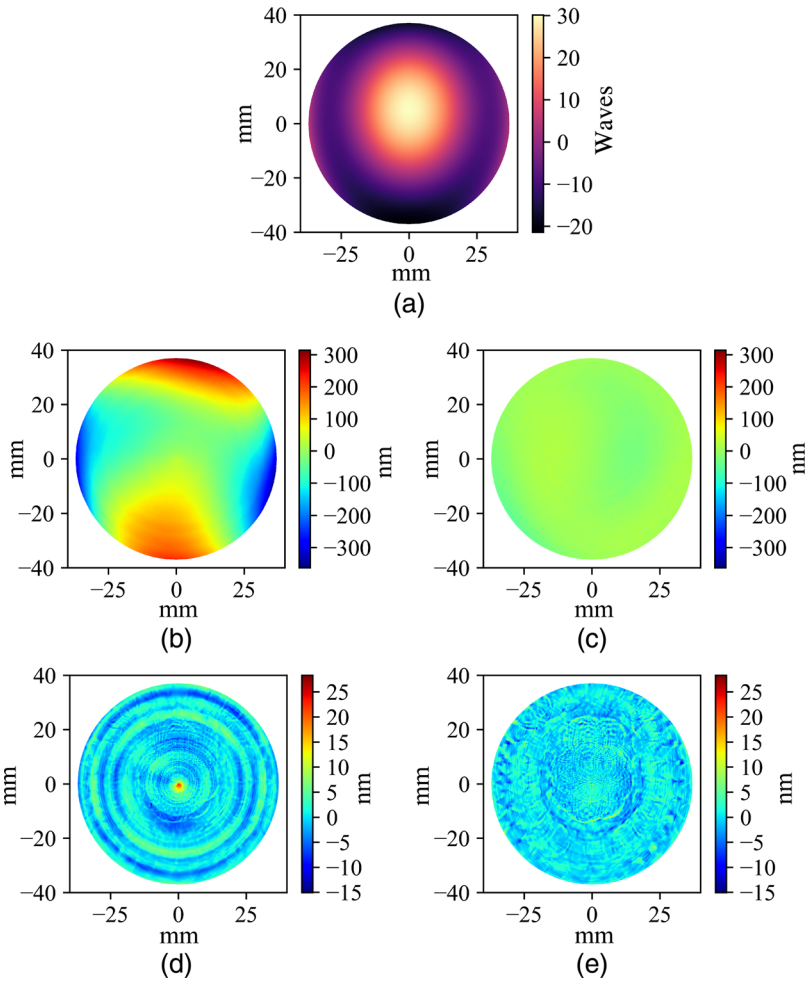

Fig. 12 (a) Mean reconstructed wavefront aberration function over the nonzero pupil amplitude. (b) Mean $\Delta \boldsymbol{z_s}$ with PTTP removed. (c) Difference in $\Delta \boldsymbol{z_s}$ from two datasets using different subaperture scan patterns. (d) Mean $\Delta \boldsymbol{z_s}$ with 36 Zernike polynomials removed to show MSF features. (e) Difference in MSF between two datasets using different subaperture scan patterns.

Figures 12(b) and 12(c) show, respectively, the mean of and difference between surface error reconstructions from two different subaperture scan patterns, with PTTP removed. The mean reconstructed surface error with PTTP removed had a P–V of 666 nm and an rms of 108 nm. The two surface reconstructions had a difference of 74 nm P–V, and 13 nm, or $\lambda/50$, rms. The surface topography error was also calculated with 36 Zernike polynomials removed to reveal MSF features. The mean MSF structure, shown in Fig. 12(d) had a P–V of 35 nm and an rms of 2.7 nm. We do not believe these MSF features are due to the subaperture translation pattern, because they were reconstructed from datasets that used both rotationally symmetric and non-rotationally symmetric subaperture scan patterns. Instead, these concentric MSF structures were likely caused by the diamond-turning process used to fabricate the test mirror. The difference in reconstructed MSF, shown in Fig. 12(e), was 25.7 nm P-V and 2.0 nm rms. These differences were largely due to reconstruction artifacts appearing near the edges of the modeled subaperture illumination patterns.

4.2 *Sources of Measurement Uncertainty*

In these measurements, system alignment is a dominant contributor to uncertainty in low-order polynomial terms. As previously discussed, PTTP were attributed to alignment and removed from the reconstructed wavefront aberration function. TTDPR is not sensitive to global piston, because a constant phase term will not affect the measured intensities. Wavefront tip-tilt will

simply shift the modeled intensity pattern relative to the detector origin due to the propagator used [Eq. (7)]. Power is sensitive to misalignments in the test configuration, specifically source-optic and optic-detector separation. Furthermore, PTTP surface terms are often included in other optical part specifications, such as center thickness (piston), wedge (tip-tilt), and radius (power).

In addition, although the nominal wavefront aberration is corrected for third-order astigmatism, astigmatism is very sensitive in this test configuration and varies as a function of mirror tilt angle θ. For example, a tilt error of 0.01 deg, or 36 arc sec, leads to a $\lambda/10$ rms wavefront error and resulting 32-nm rms surface sag error. With astigmatism removed, that induced surface error drops to 0.2 nm rms. Uncertainty in astigmatism may be reduced by measuring or calibrating the mirror tilt using more accurate equipment, such as a laser tracker. In addition, it may be possible to fabricate optical fiducials on the test mirror, outside the clear aperture, to assist in alignment. Finally, astigmatism sensitivity may be reduced by measuring the mirror in a nominally on-axis configuration, with the optical axis normal to the mirror at the surface origin. Although the overall wavefront aberration function may be larger, there should be less sensitivity to tilt errors because third-order astigmatism varies quadratically with field angle. However, an on-axis configuration would require an optical beamsplitter to avoid obscuration, which may introduce additional sources of uncertainty.

5 Conclusion

We have described the development of a surface metrology technique suitable for concave, freeform optics using TTDPR. In this measurement test configuration, optical surface measurements are possible with decreased hardware requirements, reduced sensitivity to vibration, and lack of retrace errors compared to interferometry. TTDPR wavefront-sensing performance was tested through simulation with respect to detector SNR, measurement defocus, errors in subaperture offset position, and errors in the Fourier sampling parameter, with $< \lambda/100$ rms WFSE demonstrated in most cases. Next, simulations were performed to model a full end-to-end surface measurement based on a ray-trace model of a freeform mirror under test, and surface reconstruction errors on the scale of 1 nm rms were achieved. Finally, a physical freeform mirror was measured in a tilted measurement configuration using datasets from two different subaperture scan patterns. Both form and MSF surface features were reconstructed, and surface reconstructions from two disjoint datasets were found to agree to within 13 nm rms.

Future work will focus on characterization and mitigation of error sources in this type of measurement configuration, particularly with respect to low-order terms, which are sensitive to overall system alignment. Paths for mitigating alignment-induced errors include developing compatible fiducial strategies and exploring alternative test geometries.

6 Appendix A: Translating Subaperture Illumination Model

As described previously, translating illumination was achieved by placing a circular transmission mask downstream from a point source, which projects an illumination pattern onto the surface under test. Although the transmission mask is a hard-edged stop, the projected illumination pattern will have soft edges due to diffraction effects. In addition, due to the tilted geometry, the size and shape of $A_k(x_p, y_p)$ will change as the illumination is scanned over the surface. To model $A_k(x_p, y_p)$, we first consider the mask transmittance function, $\mu(u, v)$, positioned at a distance z_1 from the point source. Let $\psi_{T,k}(u, v, z = z_1)$ be the field transmitted by the mask transmission function for each translated position, (u_k, v_k), at the $(u, v; z = z_1)$ plane

$$\psi_{T,k}(u, v; z = z_1) = \frac{1}{z_1} \exp\left[\frac{i\pi}{\lambda z_1}(u^2 + v^2)\right] \mu(u - u_k, v - v_k), \tag{20}$$

where the paraxial approximation has been applied. Next, we consider the parallel (x, y) plane, positioned at a distance z_2 from the point source, as shown in Fig. 1(b). Using the Fresnel integral, we propagate $\psi_{T,k}$ to the $(x, y; z = z_2)$ plane

$$\psi_{2,k}(x,y;z=z_2) \propto \exp\left[\frac{i\pi(x^2+y^2)}{\lambda(z_2-z_1)}\right] \iint \exp\left[\frac{i\pi}{\lambda}\left(\frac{1}{z_1}+\frac{1}{z_2-z_1}\right)(u^2+v^2)\right] \times \mu(u-u_k, v-v_k) \exp\left[\frac{-i2\pi(ux+vy)}{\lambda(z_2-z_1)}\right] \mathrm{d}u\,\mathrm{d}v. \tag{21}$$

Instead of calculating Eq. (21) directly, we use a coordinate transformation similar to one proposed by Sziklas and Siegman.[32,33] First, let us define a quantity

$$z_e = \left(\frac{1}{z_1}+\frac{1}{z_2-z_1}\right)^{-1} = \frac{z_1}{z_2}(z_2-z_1) \tag{22}$$

and introduce a change of coordinates

$$(x',y') = \left(\frac{z_e}{z_2-z_1}x, \frac{z_e}{z_2-z_1}y\right) = \left(\frac{z_1}{z_2}x, \frac{z_1}{z_2}y\right). \tag{23}$$

Equation (21) can then be simplified as

$$\psi_{2,k}\left(\frac{z_2}{z_1}x', \frac{z_2}{z_1}y'; z=z_2\right) \propto \exp\left[\frac{i\pi(x'^2+y'^2)}{\lambda}\left(\frac{z_2}{z_1^2}\right)\right] \psi'_{2,k}\left(\frac{z_2}{z_1}x', \frac{z_2}{z_1}y'; z=z_2\right), \tag{24}$$

where

$$\psi'_{2,k}\left(\frac{z_2}{z_1}x', \frac{z_2}{z_1}y'; z=z_2\right) \propto \exp\left[\frac{i2\pi(x'^2+y'^2)}{\lambda z_e}\right] \iint \exp\left[\frac{i\pi(u^2+v^2)}{\lambda z_e}\right] \times \mu(u-u_k, v-v_k) \exp\left[\frac{-i2\pi(ux'+vy')}{\lambda z_e}\right] \mathrm{d}u\,\mathrm{d}v. \tag{25}$$

The first term in $\psi_{2,k}$ is a large leading quadratic phase, i.e., the paraxial approximation of a spherical wavefront emerging from the point source, propagated a total distance z_2, appropriately scaled to the new coordinate system

$$\exp\left[\frac{i\pi(x'^2+y'^2)}{\lambda}\left(\frac{z_2}{z_1^2}\right)\right] = \exp\left[\frac{i\pi(x^2+y^2)}{\lambda z_2}\right]. \tag{26}$$

The second term, $\psi'_{2,k}$, has the form of a collimated Fresnel propagation of the mask transmittance function over an effective distance z_e with scaled output coordinates. The coordinate scaling between (x,y) and (x',y') accounts for the geometrical effect of the expanding point source. Using our definition of z_e, we can then construct an effective Fresnel number[10] for the propagation:

$$N_F = \frac{\rho^2}{\lambda z_e} = \frac{\rho^2}{\lambda(z_2-z_1)}\left(\frac{z_2}{z_1}\right), \tag{27}$$

where ρ is the physical radius of the transmission mask. Then N_F can be used to select appropriate numerical parameters for a discrete propagation, as well as provide physical intuition into the shape of $\psi'_{2,k}$.

To calculate the subaperture illumination field in the exit pupil, we use a perturbation approximation similar to that used in Sec. 2.2. We recognize the large leading quadratic component given in Eq. (26) as the accumulated phase of a nominal ray prior to interacting with the optical surface. We interpret the Fresnel propagated subaperture field, $\psi'_{2,k}$, as an amplitude and small phase perturbation on each of the nominal rays. As in Sec. 2.2, let us define a mapping function

$$(x_r, y_r) = h(x_p, y_p), \tag{28}$$

where (x_r, y_r) are the xy-plane intersection coordinates of the nominal ray that intersects the reference sphere at (x_p, y_p) and h is the mapping function. The A_k is then given as

$$A_k(x_p, y_p) = \psi'_{2,k}(x_r, y_r). \tag{29}$$

Equation (29) is an approximation of a full tilted-plane propagation. However, all propagation distances are small and the most dominant effect of the tilted propagation is a coordinate distortion, which is well modeled by the nominal ray intersections. In our work, after numerically calculating Eq. (25) using discrete Fresnel propagation, Eq. (29) was calculated using numerical interpolation. The values of $h(x_p, y_p)$, i.e., (x_r, y_r), were found numerically using a ray-trace model of the nominal test configuration.

7 Appendix B: Underlying Amplitude Model

As shown in Eq. (1), we choose to mathematically separate the exit pupil function into an amplitude component, $|g(x_p, y_p)|$, times a unit-amplitude phasor. The amplitude component of the pupil function includes the combined effects of the clipping edge of the mirror aperture and a smoothly decaying distribution caused by the spatial filter assembly. We used a pupil amplitude model, which is given as

$$|g(x_p, y_p)| = T_p(x_p, y_p) T_{\mathrm{LO}}(x_p, y_p), \tag{30}$$

where $T_p(x_p, y_p)$ is the transmittance due to the hard edge of the test mirror, and $T_{\mathrm{LO}}(x_p, y_p)$ is a superposition of low-order Zernike polynomials to model the low-frequency variations in the illumination, constrained to take purely positive values.[7] Starting from the known mirror aperture in surface coordinates, $T_M(x_s, y_s)$, the amplitude component $T_p(x_p, y_p)$ is given as

$$T_p(x_p, y_p) = T_M(x_{r,s}, y_{r,s}), \tag{31}$$

where $(x_{r,s}, y_{r,s})$ are defined by Eq. (12). The $(x_{r,s}, y_{r,s})$ were found numerically using a ray-trace model and Eq. (31) was calculated using numerical interpolation.

Acknowledgments

This research was partially supported by the National Science Foundation I/UCRC Center for Freeform Optics (IIP-1338877, IIP-1338898, IIP-1822026, and IIP-1822049). Parts of this work were previously reported in a conference proceeding.[34]

References

1. K. Fuerschbach, K. P. Thompson, and J. P. Rolland, "Interferometric measurement of a concave, ϕ-polynomial, Zernike mirror," *Opt. Lett.* **39**, 18–21 (2014).
2. P. Murphy et al., "Stitching interferometry: a flexible solution for surface metrology," *Opt. Photonics News* **14**, 38–43 (2003).
3. J. M. Rodenburg and H. M. L. Faulkner, "A phase retrieval algorithm for shifting illumination," *Appl. Phys. Lett.* **85**(20), 4795–4797 (2004).
4. G. R. Brady, M. Guizar-Sicairos, and J. R. Fienup, "Optical wavefront measurement using phase retrieval with transverse translation diversity," *Opt. Express* **17**(2), 624–639 (2009).
5. M. Guizar-Sicairos et al., "Measurement of hard x-ray lens wavefront aberrations using phase retrieval," *Appl. Phys. Lett.* **98**(11), 111108 (2011).
6. D. B. Moore and J. R. Fienup, "Subaperture translation estimation accuracy in transverse translation diversity phase retrieval," *Appl. Opt.* **55**, 2526–2536 (2016).
7. D. B. Moore and J. R. Fienup, "Ptychography for optical metrology with limited translation knowledge," *Appl. Opt.* **55**, 4596–4610 (2016).

8. A. M. Michalko and J. R. Fienup, "Transverse translation diverse phase retrieval using soft-edged illumination," *Opt. Lett.* **43**(6), 1331–1334 (2018).
9. A. M. Michalko and J. R. Fienup, "Verification of transverse translation diverse phase retrieval for concave optical metrology," *Opt. Lett.* **43**, 4827–4830 (2018).
10. J. Goodman, *Introduction to Fourier Optics*, 4th ed., W. H. Freeman and Company, New York (2017).
11. R. J. Noll, "Zernike polynomials and atmospheric turbulence," *J. Opt. Soc. Am.* **66**, 207–211 (1976).
12. Z. Hosseinimakarem, A. D. Davies, and C. J. Evans, "Zernike polynomials for mid-spatial frequency representation on optical surfaces," *Proc. SPIE* **9961**, 99610P (2016).
13. U. Grenander, *Abstract Inference*, Wiley, New York (1981).
14. G. R. Brady and J. R. Fienup, "Measurement range of phase retrieval in optical surface and wavefront metrology," *Appl. Opt.* **48**, 442–449 (2009).
15. C. Zhu et al., "Algorithm 778: L-BFGS-B: Fortran subroutines for large-scale bound-constrained optimization," *ACM Trans. Math. Software* **23**, 550–560 (1997).
16. A. S. Jurling and J. R. Fienup, "Applications of algorithmic differentiation to phase retrieval algorithms," *J. Opt. Soc. Am. A* **31**, 1348–1359 (2014).
17. M. Rimmer, "Analysis of perturbed lens systems," *Appl. Opt.* **9**, 533–537 (1970).
18. B. D. Stone, "Perturbations of optical systems," *J. Opt. Soc. Am. A* **14**, 2837–2849 (1997).
19. K. Fuerschbach, J. P. Rolland, and K. P. Thompson, "A new family of optical systems employing ϕ-polynomial surfaces," *Opt. Express* **19**, 21919–21928 (2011).
20. K. Fuerschbach et al., "Assembly of a freeform off-axis optical system employing three ϕ-polynomial Zernike mirrors," *Opt. Lett.* **39**, 2896–2899 (2014).
21. D. B. Moore and J. R. Fienup, "Extending the capture range of phase retrieval through random starting parameters," in *Front. Opt.*, OSA Technical Digest, Optical Society of America (2014).
22. J. R. Fienup et al., "Comparison of phase diversity and curvature wavefront sensing," *Proc. SPIE* **3353**, 930–940 (1998).
23. B. H. Dean and C. W. Bowers, "Diversity selection for phase-diverse phase retrieval," *J. Opt. Soc. Am. A* **20**, 1490–1504 (2003).
24. J. R. Fienup et al., "Hubble Space Telescope characterized by using phase-retrieval algorithms," *Appl. Opt.* **32**, 1747–1767 (1993).
25. J. R. Fienup, "Phase-retrieval algorithms for a complicated optical system," *Appl. Opt.* **32**, 1737–1746 (1993).
26. M. Guizar-Sicairos and J. R. Fienup, "Image reconstruction by phase retrieval with transverse translation diversity," *Proc. SPIE* **7076**, 70760A (2008).
27. M. Guizar-Sicairos and J. R. Fienup, "Phase retrieval with transverse translation diversity: a nonlinear optimization approach," *Opt. Express* **16**, 7264–7278 (2008).
28. R. Kingslake, "Who discovered Coddington's equations?" *Opt. Photonics News* **5**, 20–23 (1994).
29. K. Fuerschbach, "Freeform, ϕ-polynomial optical surfaces: optical design, fabrication and assembly," PhD Thesis, University of Rochester, Rochester, New York (2014).
30. A. S. Jurling and J. R. Fienup, "Phase retrieval with unknown sampling factors via the two-dimensional chirp Z-transform," *J. Opt. Soc. Am. A* **31**, 1904–1911 (2014).
31. R. Soummer et al., "Fast computation of Lyot-style coronagraph propagation," *Opt. Express* **15**, 15935–15951 (2007).
32. E. A. Sziklas and A. E. Siegman, "Mode calculations in unstable resonators with flowing saturable gain. 2: fast Fourier transform method," *Appl. Opt.* **14**, 1874–1889 (1975).
33. A. Siegman, *Lasers*, University Science Books, Mill Valley, California (1986).
34. A. M. Michalko and J. R. Fienup, "Sensitivity study of transverse translation diverse phase retrieval for freeform metrology," *Proc. SPIE* **10742**, 107420T (2018).

Aaron M. Michalko received his Bachelor of Science in optical engineering from the Institute of Optics at the University of Rochester in 2014. Currently, he is a PhD candidate in optics at

the University of Rochester. His research interests include optical metrology, phase retrieval, and image-based wavefront sensing.

James R. Fienup received his AB from Holy Cross College, and MS degree and PhD in applied physics from Stanford University, where he was a National Science Foundation graduate fellow. After performing research at ERIM, he became the Robert E. Hopkins Professor of Optics at the University of Rochester. He is a fellow of SPIE and OSA, a member of the National Academy of Engineering, and a recipient of SPIE's Rudolf Kingslake Medal and Prize.